Full-depth desalination of warm sea ice

Fernanda Jardon, Frédéric Vivier, Martin Vancoppenolle, Antonio Lourenço, Pascale Bouruet-Aubertot, Yannis Cuypers

JOURNAL OF GEOPHYSICAL RESEARCH: OCEANS, VOL. 118, 435–447, doi:10.1029/2012JC007962, 2013

Full-depth desalination of warm sea ice

F. P. Jardon,[1] F. Vivier,[1] M. Vancoppenolle,[2,3] A. Lourenço,[1] P. Bouruet-Aubertot,[1] and Y. Cuypers[1]

Received 7 February 2012; revised 27 September 2012; accepted 21 November 2012; published 31 January 2013.

[1] The large-scale Arctic sea-ice retreat induces a gradual replacement of thick, multi-year sea ice by thinner first-year ice. The latter has distinctive physical properties and is in particular substantially saltier. It is generally thought that while salt rejection occurs primarily during ice formation in winter, most of the remaining brine is flushed out of the ice by the percolating surface melt water in summer. Here, it is argued that a substantial part of this residual desalination of first-year sea ice can occur well before summer melt, due to brine convection over the full thickness of the ice, once the ice temperature is higher than a threshold that depends on bulk salinity and thickness. This critical temperature is substantially higher than the permeability threshold. The argument stems from a theoretical analysis of the porous Rayleigh number depicting the propensity for convection in the mushy-layer theory. It is supported by simulations performed with a state-of-the-art 1-D sea-ice model. The study was initially motivated by observations collected in March 2007 in Storfjorden, Svalbard. Those are indirect, however, and are thus presented here as a possible example. Two sporadic anomalies of seawater salinity were recorded close to the base of 40 cm thick ice in temperature conditions that are incompatible with ice formation. Analyses and simulations forced with observed atmospheric conditions suggest that the second peak is caused by flushing of meltwater, while the first and most intense peak is likely associated with an episode of brine convection over the full depth of the ice, yielding significant desalination.

Citation: Jardon, F. P., F. Vivier, M. Vancoppenolle, A. Lourenço, P. Bouruet-Aubertot, and Y. Cuypers (2013), Full-depth desalination of warm sea ice, *J. Geophys. Res. Oceans*, *118*, 435–447, doi: 10.1029/2012JC007962.

1. Introduction

[2] Arctic sea ice is profoundly changing. The reduction in summer sea-ice extent evidenced by satellite data since the 1980s [e.g., *Comiso*, 2002], which has accelerated in the past few years with a series of record minima [*Stroeve et al*., 2007; *Comiso et al*., 2008], occurs primarily at the expense of thick multi-year ice. The decline in sea-ice extent is indeed accompanied by a nearly 50% reduction of the average sea-ice thickness, from 3.64 m in the 1980s to 1.89 m in 2009, for winter conditions [*Kwok and Rothrock*, 2009]. This thinning mostly reflects the replacement of multi-year ice by first-year ice [*Haas et al*., 2010]. Indeed, the average age of the sea ice has dramatically decreased, particularly as a result of recent regime shifts [Rigor and Wallace, 2004; *Maslanik et al*., 2007; *Nghiem et al*., 2007]. Recently, *Maslanik et al*. [2011] have shown that multi-year ice now represents only 45% of the total ice extent in March, while it was 75% in the mid-1980s.

[3] The transition from a perennial to a seasonal Arctic sea ice cover will likely feedback on climate by changing atmosphere-ice-ocean heat, salt, and freshwater fluxes [*Holland et al*., 2006]. This shift toward thinner seasonal ice already suggests a coincident decrease in surface albedo and an increase of solar energy absorption by the ice-ocean system during summer melt [*Perovich et al*., 2002, 2007; *Nghiem et al*., 2007]. Multi-year ice has lower brine content and is fresher than first-year ice [e.g., *Weeks and Ackley*, 1986], since it has undergone summer melt. Investigating the release of salt from first-year ice is therefore highly suited to the Arctic where the ice cover is transitioning toward a seasonal cover.

[4] About two thirds of the initial seawater salt content is rejected during early ice growth [e.g., *Kovacs*, 1996]. Because the ice crystalline lattice hardly tolerates impurities, the remaining salt is nearly exclusively contained in liquid brine inclusions. Due to brine rejection, ice loses most of its salt during its first year [e.g., *Kovacs*, 1996]. First-year (FY) sea ice has therefore a distinct salinity profile compared with older ice, which greatly affects brine volume fraction (or porosity), e, and thermal properties. The ice enthalpy and thermal conductivity both decrease with increasing salinity for a given temperature, whereas the heat capacity increases [*Malmgren*, 1927].

[1]Laboratoire d'Océanographie et du Climat (LOCEAN)-IPSL, Université Pierre et Marie Curie, Paris, France.
[2]Georges Lemaître Centre for Earth and Climate Research, Earth and Life Institute, Université catholique de Louvain, Louvain-la-Neuve, Belgium.
[3]Dept. of Atmospheric Sciences, University of Washington, Seattle, WA, USA.

Corresponding author: F. P. Jardon, Laboratoire d'Océanographie et du Climat - Institut Pierre-Simon Laplace, Université Pierre et Marie Curie, 4 Place jussieu, Tour 45/55, 4ème étage, boîte 100, Paris, 75005, France. (Fernanda.Jardon@locean-ipsl.upmc.fr)

2169-9275/13/2012JC007962

[5] Porosity provides a primary control on fluid transport within the sea ice as it determines fluid permeability. Applying percolation theory to sea ice, *Golden et al*. [1998] suggested that ice is permeable above a critical porosity threshold of $e=5\%$. For a typical bulk salinity S_i of 5 (throughout this paper, salinities are expressed relative to the practical salinity scale PSS-78 and are thus dimensionless), ice is therefore permeable when temperature T_i exceeds −5 °C (based on the liquidus relation). This rule was referred to as the "rule of fives" by *Golden et al*. [1998].

[6] Among the various processes for potentially removing salt from sea ice [*Untersteiner*, 1968; *Cox and Weeks*, 1974; *Eide and Martin*, 1975], recent studies confirmed that only gravity drainage and flushing contribute significantly [*Notz and Worster*, 2009; *Weeks*, 2010; *Hunke et al*., 2001]. Gravity drainage results from the convection of dense, saline brine through permeable ice in a vertical temperature gradient, with colder temperatures on the top. This temperature gradient involves an unstable brine salinity gradient to maintain phase equilibrium. Convection develops once available potential energy (i.e., negative buoyancy) overcomes viscous dissipation, or, quantitatively, once a porous-medium Rayleigh number (*Ra*) exceeds a critical value $Ra_c \approx 10$ [*Notz and Worster*, 2008]. This formulation stems from mushy-layer theory [*Feltham et al*., 2006; *Wettlaufer et al*., 1997a; *Worster*, 1997], where a mushy layer is defined as a two-phase (solid ice and brine), two-component, reactive porous medium. Flushing refers to the washing out of brine by the percolation of surface meltwater through the permeable ice matrix in response to a hydrostatic head.

[7] Desalination of sea ice has frequently been observed to be associated with gravity drainage during sea-ice formation [e.g., *Lake and Lewis*, 1970; *Notz and Worster*, 2008] or with flushing during the melt season [e.g., *Trodahl et al*., 2000; *Freitag and Eicken*, 2003; *Vancoppenolle et al*., 2007]. According to these studies [see also *Wettlaufer et al*. 1997a], winter desalination occurs through gravity drainage, whereby convection seems to develop in a thin (~5 cm) layer near the ice base. Convection over much wider vertical scales has been inferred from temperature data [*Pringle et al*., 2007] or associated with the freezing of slush above a permeable ice layer [*Lytle and Ackley*, 1996]. In contrast, observations of salinity peaks in the upper ocean associated with brine release from sea ice are relatively sparse. *Hudier et al*. [1995] reported salt rejection at the base of the ice that they associate with an upward flushing of sea water. More recently, *Widell et al*. [2006] observed a basal salt flux from warming first-year sea ice in the Svalbard region in spring time, which was correlated with the ocean-ice heat flux.

[8] In this work, we argue that a substantial fraction of the residual salt remaining in first-year sea ice can be rejected well before summer, due to gravity drainage developing throughout the full thickness of the ice, once the ice is warmer than a temperature threshold dependent on bulk salinity and thickness. This threshold is well above the permeability threshold. This argument stems from theoretical and modeling considerations but was initially motivated by observations. The latter are indirect; however, two sporadic positive anomalies in seawater salinity were recorded close to the base of the ice in March 2007, near the end of the freezing season, in conditions incompatible with ice formation. Measurements were taken in Storfjorden, a large fjord of the Svalbard Archipelago that hosts a latent heat polynya [*Haarpaintner et al*., 2001; *Skogseth et al*., 2004], which is prone to the formation of substantial amounts of young ice.

[9] This paper is structured as follows. In section 2, we derive from theory a necessary condition for gravity drainage to occur over the entire thickness of the ice. Idealized simulations performed with a 1-D sea-ice model, including a state-of-the-art parameterization of salt dynamics, are conducted in section 3 to illustrate theoretical results. We then present in section 4 our observations as a possible example of full-depth gravity drainage. Observations show two salinity peaks occurring 10 h apart during a warm storm, the second of which is associated with flushing as indicated by model simulations. Modeling further suggests that the first and most intense peak is caused by gravity drainage occurring over the full depth of the ice. A concluding discussion follows in section 5.

2. Theory

[10] In the introduction, we claimed that gravity drainage may not be limited to the lowermost fraction of the ice layer and that in some circumstances it could lead to substantial desalination of the ice by the downward transport of salt throughout the full thickness of the ice.

[11] Here, we examine under which environmental conditions full-depth convection would be possible. Specifically, we analyze the sensitivity of brine convection to the temperature of the sea ice and derive a necessary condition for convection over the entire ice column. This condition is expressed as a temperature threshold that depends on the bulk salinity and thickness of the ice.

[12] The propensity for brine convection (or gravity drainage) in sea ice is compactly described by mushy-layer theory [*Worster*, 1992; *Feltham et al*., 2006] using a porous-medium Rayleigh number, *Ra* [*Worster*, 1992; *Wettlaufer et al*., 1997a; *Notz and Worster*, 2008]. This number reflects the ratio between the energy available for convection and the energy that is dissipated during convection, owing both to the moving brine's viscosity and to thermal energy loss through heat diffusion. The expression used here for *Ra* depends on the vertical coordinate in the ice, as per *Notz and Worster* [2008], and reads

$$Ra = \frac{g(h_i - z)\rho_w \beta_w (S_{br} - S_w)\Pi(e_{\min})}{\kappa \eta}, \qquad (1)$$

where g is the gravitational acceleration; $h_i - z$ is the distance between a given level in the sea ice z and the base of the ice at depth h_i; $\rho_w \beta_w (S_{br} - S_w)$ is the difference between the brine density at level z (with salinity S_{br}) and that of the seawater (with salinity S_w); while $\Pi(e_{\min})$ represents the effective sea-ice permeability (in square meters), computed as a function of the minimum brine volume fraction $e_{\min}$ between level z and the base of the ice. Finally, κ and η are the thermal diffusivity and dynamic viscosity of the liquid brine, respectively [*Wettlaufer et al*., 1997b; *Notz and Worster*, 2008]. These studies assume that thermodynamical equilibrium is not maintained on the fast time scales associated with convection (Dirk Notz, personal communication). The thermal diffusivity of the moving liquid brine (which is one order smaller than that of the surrounding freshwater ice) is therefore used

in (1), rather than the bulk diffusivity of ice. Convection is triggered when the available potential energy (negative buoyancy) overcomes dissipation by a factor of ≈10 (the critical Rayleigh number, Ra_c) [*Notz and Worster*, 2008]. The dependence of the effective permeability on the brine volume fraction is taken as $\Pi(e)=10^{-17}(10^3\times e)^{3.1}$, an empirical relationship derived by *Freitag* [1999]. A cubic dependence on the porosity is predicted by the Kozeny-Carman equation, which models a porous material as an assembly of capillary tubes [*Kozeny*, 1927; *Carman*, 1937]. Cubic dependence is also demonstrated theoretically for a hierarchical model [*Golden et al.*, 2007].

[13] To analyze the sensitivity of *Ra* on sea-ice temperature T_i, we explicitly introduce this variable in (1). The numerator of (1) is the product of the driving density gradient and permeability, which inversely depend on T_i. Competing effects are therefore expected when temperature increases. Brine salinity, S_{br}, is constrained by the liquidus relationship, which is expressed as a third order polynomial in temperature [*Assur*, 1958]

$$S_{br}(T_i) = -1.2-21.8T_i-0.919T_i^2-0.0178T_i^3. \quad (2)$$

[14] For T_i warmer than ~−6°C, the latter equation is well approximated by the linear relation $S_{br}(T_i)\approx -T_i/\mu$, where $\mu=0.054\,°C‰^{-1}$, which shows the direct dependence of the driving density gradient on T_i. Conversely, because the bulk salinity of the ice S_i is related to the brine salinity according to $S_i=S_{br}\times e$, one can write $e(S_i,T_i)\approx -\mu S_i/T_i$, showing that brine volume *e* and permeability depend on the inverse of T_i.

[15] Figure 1a displays $Ra(T_i)$ for different values of S_i, assumed to be vertically uniform for simplicity, ranging between 5 and 10 (colored solid lines), and for a distance

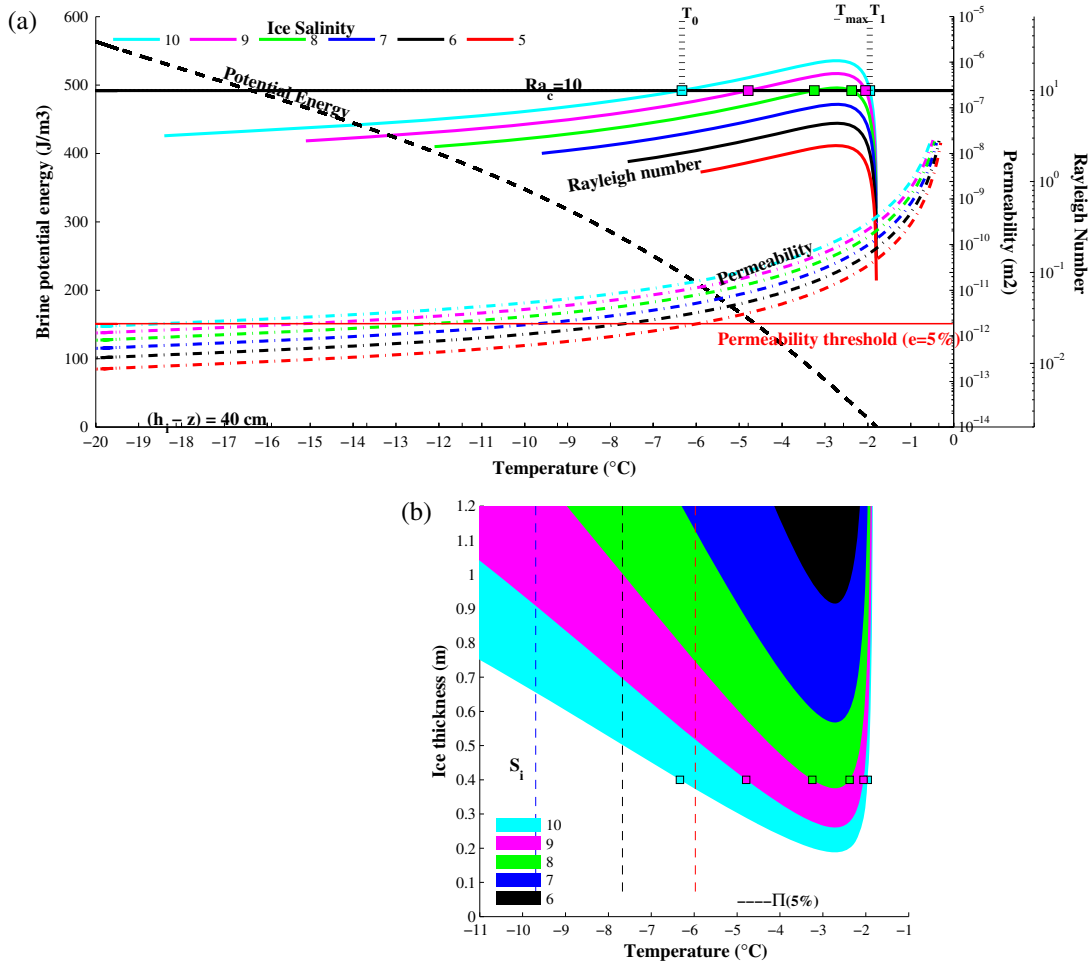

Figure 1. (a) Rayleigh number (*Ra*) as a function of temperature for 40 cm thick ice with different bulk salinities (from 5 to 10). Also shown are the contributions from the driving buoyancy (black dashed line, left axis) and permeability (colored dashed lines, right axis) at the numerator of *Ra*. The red line indicates the permeability threshold corresponding to a brine volume fraction of 5%, and the black line denotes the critical *Ra* of 10, which defines a temperature interval $[T_0,T_1]$ outside of which convection is impossible. (b) Surfaces of Rayleigh number exceeding 10 as a function of ice thickness and temperature, for a bulk salinity ranging between 5 and 10. The colored areas denote regions where brine convection is possible. Vertical dashed lines indicate the temperature below which ice is impermeable for a given salinity, based on a brine volume fraction threshold of 5%.

into the ice ($h_i - z$)—or equivalently an ice thickness—of 40 cm. In this computation, we used $\kappa = 1.2 \times 10^{-7} m^2 s^{-1}$ and $\eta = 2.55 \times 10^{-3}$ kg m$^{-1}s^{-1}$, consistent with *Notz and Worster* [2008], while (2) was used for the liquidus. T_i represents the temperature at level $h_i - z$ (equivalently at the surface), and we assume that the brine volume is minimal there, which enables to express the permeability as a function of T_i. Doing so, it is implicitly assumed that the ice temperature is higher for layers located underneath, which is a reasonable assumption (rigorously exact for stationary conditions). Also shown in Figure 1 are the contributions of the two terms in the numerator of (1), the driving buoyancy displayed as brine potential energy (black dashed line, left axis), and the permeability (colored dashed lines, right axis). For cold temperatures, the brine is saltier and denser, enhancing the driving buoyancy term, whereas the ice permeability diminishes, enhancing the resistance to fluid motion. As mentioned in section 1, ice becomes practically impermeable for e smaller than 5%. This corresponds to a permeability smaller than $1.85 \times 10^{-12} m^2$ (red horizontal line in the figure) in the formulation of *Freitag* [1999]. This formulation does not have a permeability cutoff at a brine volume of 5%, but we assume the permeability is zero below this brine volume, which, in practice, means that sea ice is impermeable. Accordingly, the set of Ra curves are truncated in the temperature range when sea ice is permeable. The $Ra(T_i)$ curves all display similar variations, increasing with temperature until reaching a maximum for $T_i = T_{\max}$ (a value independent of ice thickness) before decreasing abruptly. We find that $T_{\max} \approx 1.42 T_f$, where T_f is the freezing temperature. The critical Rayleigh number for the onset of gravity drainage ($Ra_c \approx 10$) is indicated by the horizontal black line: this defines an interval $[T_0, T_1]$, bracketing $T_{\max}$, outside of which convection is impossible under the assumptions mentioned above. It can be seen from the figure that, owing to the control of porosity, convection occurs for relatively warm sea ice.

[16] Similar graphs can be constructed for different ice thicknesses. The envelope of intervals $[T_0, T_1]$ is reported in Figure 1b, for S_i ranging between 5 and 10, and for distances in the ice (or ice thickness) ranging between 0 and 1.2 m. This figure summarizes the minimal sea-ice surface temperature required for convection to occur over the full thickness, given the initial bulk salinity of sea ice, assumed to be vertically uniform here. It is instructive to interpret this figure using examples. For ice 40 cm thick, the cyan symbol in Figure 1b indicates that convection can occur ($Ra > 10$) over the entire ice thickness as soon as T_i exceeds ~−6.3 °C, assuming surface ice salinity of 10. Note that this temperature threshold far exceeds the temperature permeability threshold of $T_i = -18$ °C, corresponding to $e = 5\%$ for $S_i = 10$ (this permeability threshold rises to −12 °C, if assuming instead the linear liquidus relation). This figure additionally shows that for a given ice thickness, full-depth convection can only occur for certain values of ice salinity. For example, for an ice thickness of 40 cm, surface bulk salinity must be at least 8 for full-depth convection to occur, while it is impossible with an ice salinity of 7 (the corresponding dark blue surface in the figure does not reach the ordinate of 40 cm). Instead, for $S_i = 7$, ice has to be both thicker (~56 cm) and warmer (~−3 °C) to enable full-depth convection. In all cases, the temperature threshold for full-depth convection is higher than the permeability threshold.

[17] Note that the existence of a temperature threshold for convection (for a given depth of convection and ice salinity) is analogous to the existence of a critical depth for the onset of convection in growing sea ice, as evidenced from laboratory experiments by *Wettlaufer et al*. [1997a]. In the latter case, however, it is the increase in potential energy that is responsible for reaching a supercritical Ra triggering convection, while in our case, convection is triggered by the decrease in dissipated energy with increasing temperature.

3. Idealized Simulations

[18] The purpose of this section is to illustrate the theoretical results of section 2 through idealized numerical simulations, whereby we examine the occurrence of full-thickness desalination of the ice as a function of sea-ice temperature. Simulations are conducted using the state-of-the-art 1-D halo-thermodynamic sea-ice model LIM1D developed by *Vancoppenolle et al*. [2010], which is first briefly introduced. The results of three runs with synthetic surface forcings yielding different thermal fields within the ice are then presented.

3.1. The 1-D Halo-Thermodynamic Sea-Ice Model

[19] The thermodynamic component of the model is from *Vancoppenolle et al*. [2007], based on the *Bitz and Lipscomb* [1999] energy-conserving model. Ice growth and melt rates are computed using the balance between atmospheric, oceanic, and conductive heat fluxes. The temperature, which is the solution of the heat diffusion equation in one layer of snow and 20 layers of sea ice, determines conductive fluxes. The halodynamic module stems from a simplification of the exhaustive mushy-layer theory and is formulated in terms of an advection-diffusion equation solved for brine salinity, assuming a purely vertical brine motion [*Vancoppenolle et al*., 2010]:

$$\frac{\partial}{\partial t}[eS_{br}] = -ev_z \frac{\partial S_{br}}{\partial z} + \frac{\partial}{\partial z}\left[D_\sigma \frac{\partial S_{br}}{\partial z}\right]. \quad (3)$$

[20] The first term on the right-hand side of (3) accounts for flushing, represented as an advective flow (with velocity v_z) triggered by surface meltwater availability and the condition $e \geq 5\%$ over the entire sea-ice column. Gravity drainage is represented using a diffusion term, whereby salt diffusivity $D_\sigma(Ra)$ is parameterized to increase from the molecular value D_σ^{mol} to a much larger turbulent value, D_σ^{tur}, when Ra reaches the critical value of ~10, in order to mimic brine convection. For numerical reasons, the sharp transition of $D_\sigma(Ra)$ around the critical Ra is continuous, formulated as a hyperbolic tangent. Note that in the model, as in the theoretical analysis of section 2, Ra refers to the local Rayleigh number (see equation 1), which depends on the elevation of each sea-ice layer above the bottom interface of the ice.

[21] Sensitivity tests were performed by *Vancoppenolle et al*. [2010] from which they concluded that the turbulent salt diffusivity D_σ^{tur} has to be at least $10^{-7} m^2 s^{-1}$. Here, D_σ^{tur} is set to $3 \times 10^{-7} m^2 s^{-1}$, which is nearly three orders of magnitude larger than the molecular value of $D_\sigma^{\mathrm{mol}} = 6.8 \times 10^{-10} m^2 s^{-1}$. This value gives similar desalination rates for a time step of 1 h as the $1 \times 10^{-6} m^2 s^{-1}$ proposed by *Vancoppenolle et al*.

[2010] for a time step of 1 day. In the present configuration, unless otherwise noted, model parameters are the same as in *Vancoppenolle et al.* [2010].

3.2. Simulations: Full-Depth Desalination Driven by Air Temperature Changes

[22] The purpose of the numerical experiments is to test the dependency of sea-ice desalination on the ice temperature field. Three different simulations are conducted: in the first one (Run I), the sea-ice temperature, T_i, is kept below the permeability threshold T_{perm} at all times ($-\mu S_i/T_{\mathrm{perm}}=5\%$ for the linear approximation of the liquidus relation); in the second one (Run II), T_i is brought above the permeability threshold T_{perm}, but kept below the surface temperature criterion for full-depth convection as derived in section 2; and in the third simulation (Run III), T_i is brought above this latter threshold. The model internal temperature field of the three experiments is achieved by prescribing different evolutions in air temperature, while the other forcing variables (pressure, wind speed, cloud fraction, and snowfall) are kept constant (their values provided in Table 1). Those forcing variables are used to compute the components of the surface energy budget. All model simulations start on 8 March and end on April 10 for the solar radiation to be representative of spring conditions. Radiative and turbulent fluxes over the ice are computed from the forcing module of the sea-ice model, based on parameterizations described in *Vancoppenolle et al.* [2011]. The solar radiation is computed as a function of the solar zenith angle (function of latitude and day of the year), specific humidity, and cloud fraction [*Shine*, 1984]. The net long-wave heat flux is estimated based on the Berliand bulk formula [*Berliand and Berliand*, 1952] using air temperature, surface temperature, relative humidity, and cloudiness factor. Finally, turbulent fluxes of latent and sensible heat are computed as per *Goosse* [1997], based on classical bulk aerodynamic formulas. In this formulation, drag coefficients are assumed constant over the sea ice and equal to 1.75×10^{-3} [*Parkinson and Washington*, 1979; *Maykut*, 1982]. This assumption does not significantly modify the results [*Goosse*, 1997].

[23] The prescribed air temperature is shown in Figure 2a for the three simulations. It is kept constant at −28 °C for Run I. For Run II, the air temperature increases linearly after 150 hourly time steps from −28 °C, reaching a plateau of −20 °C after 6 h. Run III includes a final temperature increase 100 h after the first transition, up to a plateau of −7.5 °C.

[24] The model initial conditions are $h_i=3$ cm for ice thickness, $h_s=1$ cm for snow depth, and $S_i=12$ for the bulk salinity, constant with depth. The initial temperature profile within the ice and snow is linear, with basal temperature at the seawater freezing point of $T_w=-\mu S_w$, where $S_w=34.15$.

Table 1. List of Constant Values for the Variables Needed to Force the Model

Variable	Value	Units
Atmospheric pressure	100,000	Pa
Wind speed	5.0	ms^{-1}
Specific humidity	5.76×10^{-4}	gkg^{-1}
Cloud fraction	0.9	–
Snow fall	0	mmh^{-1}
Ocean heat flux	5	Wm^{-2}

[25] The results of the three simulations are shown in Figure 2b for T_i, Figure 2c for S_i, and Figure 2d for the ice-ocean salt flux. The values of the different plateaux for air temperature were tuned to obtain surface sea-ice temperatures in agreement with the threshold values discussed in the theoretical analysis, taking into account the evolution of surface bulk salinity. For Run I, the upper layers of the thickening sea-ice cool off enough to become impermeable after a few days. The initial stage of ice growth when ice is thin and permeable is disregarded here. Continuous ice growth is observed along the simulation (70 cm over 1 month), which, after an initial adjustment phase, yields an ice-ocean salt flux $\sim5\times10^{-6}\mathrm{kg\ m}^{-2}s^{-1}$ (Figure 2d, left). The bulk salinity (Figure 2c, left) adjusts from the vertically uniform initial value to a C-shape profile characteristic of Arctic first-year ice [e.g., *Cox and Weeks*, 1988]. For Run II, after the first transition in the forcing, the surface ice temperature reaches −11 °C, thus exceeding the permeability threshold corresponding to the surface bulk salinity (Figure 2b, middle). Due to the warmer air temperature, the ice grows more slowly after the plateau, leading to a reduction in the ice-ocean salt flux. There is no dramatic change in bulk salinity evolution compared with Run I, which still exhibits a C-shaped profile after the air temperature plateau. In particular, no brine convection is observed above the bottom permeable layer, where *Ra* remains subcritical.

[26] In contrast, for Run III, convection starts after the second transition in the forcing, which occurs when the ice is ~40 cm thick, and the surface bulk salinity is ~10.5. Surface ice temperature rises above −6 °C, exceeding the convection threshold, which according to Figure 1b, is around −6.3 °C, for 40 cm thick ice with a salinity of 10 (cyan square in this figure). This increase in surface ice temperature enables the rapid cascading of salt throughout the full thickness of the ice, as is visible in Figure 2c (right). The Rayleigh number becomes supercritical during this episode within all the model ice layers, as denoted by the isoline $Ra=10$ in the figure, confirming the occurrence of gravity drainage. This yields a significant desalination of the ice column, whose vertically averaged bulk salinity (excluding the few centimeters near the ice base) decreases from ~10 or higher to 7 after this episode (a salt loss of ~30% for this single event). Accordingly, a sharp peak reaching $3\times10^{-5}\mathrm{kg\ m}^{-2}s^{-1}$ is observed in the ice-ocean salt flux during this episode (Figure 2d, right).

4. Indirect Evidence of Desalination From Observations

[27] The theoretical arguments, as well as the idealized simulations of the previous sections, suggest that gravity drainage over the full thickness of the ice is possible once ice is warm enough, as summarized in Figure 1b, provided that the ice has sufficient initial bulk salinity. We report here serendipitous observations of salinity anomalies at the base of relatively warm ice in Storfjorden, Svalbard, as a possible example of such full-thickness gravity drainage. Because these observations are indirect, we have performed simulations with the halo-thermodynamic sea-ice model, forced with observed atmospheric conditions (see section 4.2), further testing the sensitivity of brine release to initial conditions.

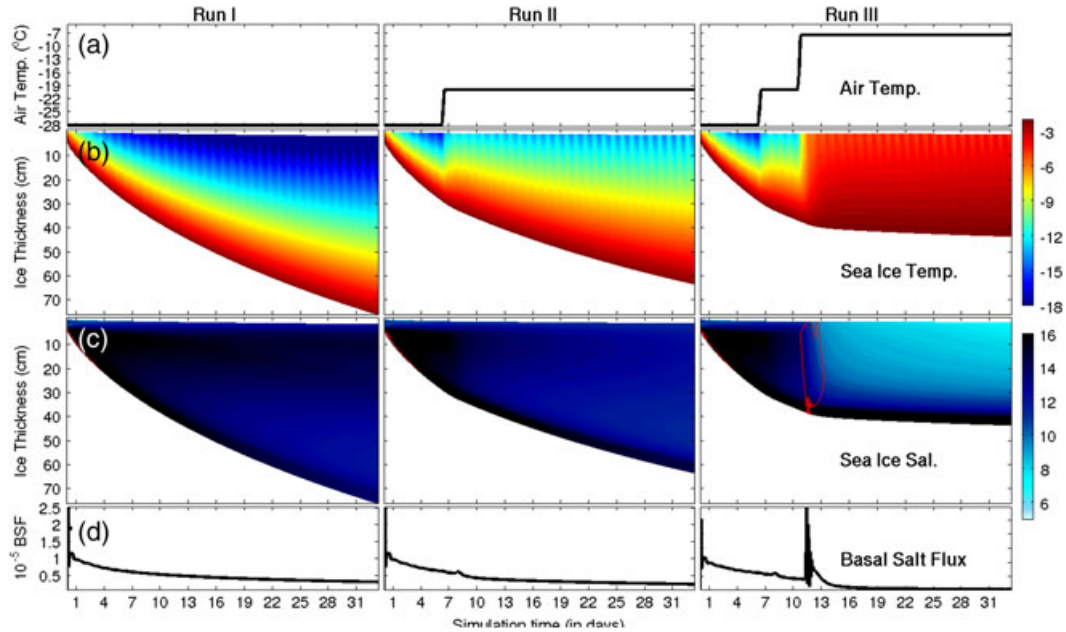

Figure 2. Time series of (a) air temperature (°C), (b) sea-ice temperature (°C), (c) sea-ice salinity and contours of critical Rayleigh number (Ra_c=10, red line), and (d) basal salt flux (kg m$^{-2}s^{-1}$]) for three distinct simulations: Run I, Run II, and Run III (see text for details).

4.1. Observations

4.1.1. Experimental Setup and Data

[28] In late March 2007, an ice-tethered mooring, equipped with autonomous CTD (conductivity-temperature-depth) sensors for recording temperature and salinity every 2 min at five vertical levels (1.8, 10, 20, 30, and 55 m) was deployed in Storfjorden, Svalbard (Figure 3), together with a prototype buoy developed at LOCEAN, "Ice-T," for measuring in particular ice thickness and thermal profiles in the sea ice [*Vivier et al.*, 2013]. The main objective of this experiment was to document dense water formation in the polynya and analyze high-frequency ocean dynamics and associated turbulent mixing [*Jardon et al.*, 2011, 2012]. The experimental setup was installed in 40 cm thick sea ice with slightly positive freeboard (<1 cm), covered by ~20 cm of snow. The mooring and the buoy were fixed 7 m apart into 50 cm diameter holes drilled into the ice, partially filled with a snow-ice mixture in order to keep the buoys vertical.

[29] The whole experiment lasted 10 days, from 23 March to 2 April (day of the year 2007 82.75 to 92.32). However, a warm storm occurred during deployment that eventually broke the ice the next day, setting the instruments adrift. Here, we focus on the unexpected salinity signals recorded at 1.8 m depth during this first day of measurements, before the ice cover had broken. Unfortunately, because salt dynamics within the ice were not the initial scope of the experiment, neither snow nor ice properties (in particular

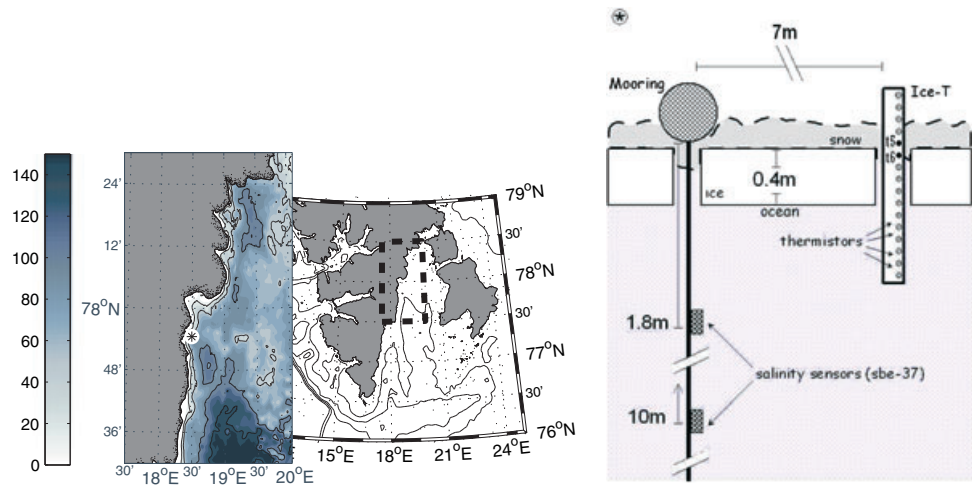

Figure 3. Storfjorden, Svalbard (left). Instrument location shown in the inset. Sketch of the experimental setup (right).

density and salinity) were measured during deployment. The accuracy of salinity measurements in sea water is 0.003 [see *Jardon et al*., 2011 for more details on the experiment's set up and the instruments' precision].

[30] Hourly air temperature, wind, and atmospheric pressure data were recorded less than 10 km away at the polar yacht Vagabond, which was wintering in the fjord as part of the EU DAMOCLES project. Additional variables (relative humidity, snowfall and cloud fraction) needed to compute heat fluxes and to force the model come from the ECMWF ERA-interim reanalysis [*Simmons et al*., 2006] at a spatial resolution of 0.75°, available every 6 h. The consistency between reanalysis and observed data has been checked [*Jardon et al*., 2012]. This set of atmospheric data is used in the forcing formulas described in section 3.2. Regarding the ocean-ice heat flux, seawater was slightly supercooled (temperature of -1.935 ± 0.005 °C, nearly vertically uniform, slightly below the in situ freezing point) down to 30 m [*Jardon et al*., 2012], hence no heat was available from the ocean. Therefore, the ocean heat flux is set to 0 $\mathrm{W\,m^{-2}}$.

4.1.2. Results

[31] Two positive salinity anomalies, reaching 0.41 (*S*1) and 0.21 (*S*2) with respect to the average seawater salinity (S_w) of 35.17, were observed 1.4 m below the sea ice (Figure 4). These anomalies occurred in two short episodes of ~1 h for *S*1 and 20 min for *S*2. Their origin is investigated hereafter.

[32] These observations are probably not an instrumental artifact. Ice formation under windy conditions, as is typically observed in Storfjorden, can lead to the presence of frazil ice crystals. The intrusion of small frazil crystals in the conductivity cell could affect the seawater salinity measurements; but their effect is, on the contrary, to underestimate the actual seawater salinity [*Skogseth et al*., 2009]. Interestingly, these salinity signals are barely observable by the sensor at 10 m or by the sensors located at greater depth (not shown).

[33] It is possible that surface salinity anomalies are related to lateral advection, although it does not seem clear why in this case they could not be observed with comparable intensity at 10 m or deeper. Furthermore, the sporadic character of both signals makes quite unlikely the hypothesis that there was horizontal inflow of water with higher salinity (one might expect a more persistent signature from the interception of a mesoscale or even submesoscale structure). A more likely cause for salinity increase near the base of the ice is brine rejection by the ice, and we investigate in the remainder of this section the consistency of this hypothesis, as well as the rejection mechanism at play.

[34] Most brine rejection occurs during sea-ice formation, which requires heat loss from the ocean. Here, a warm storm associated with westerly winds occurred during the observation period. The air temperature increased and became positive immediately after the first salinity signal *S*1 (Figure 5a). The temperature reached a maximum value of 7 °C about 1.5 h before *S*2 and finally decreased to below 0 °C at the end of day 83, well after the two episodes. Accordingly, the net atmospheric heat flux (Q_{net}) shows a strong increase starting during event *S*1 and continuing over *S*2 (Figure 5b). Note that during the preceding week, intense northeasterly winds that brought about cold air masses (Figure 5a) opened the polynya [*Jardon et al*., 2012, Figure 6]. This yielded an intense heat loss, as large as $\sim -390\,\mathrm{W\,m^{-2}}$ over the open water areas ($-60\,\mathrm{W\,m^{-2}}$ over ice on day 78; Figure 5b), resulting in the large production of frazil ice in Storfjorden, on the order of 2 $\mathrm{km^3}$. These cold atmospheric conditions caused the supercooling of the seawater, observed down to 30 m [*Jardon et al*., 2012], thus cutting any supply of heat from the ocean to the ice at the time of the observations.

[35] Although ice could not grow due to a heat loss to the atmosphere at the time of the observations, vertical heat conduction in the ice interior could nevertheless produce basal ice growth. This kind of process was, for example, observed in early summer in the Canadian Archipelago over thick sea ice [*Polashenski et al*., 2011]. This is likely not the case here since the sea ice is too thin (40 cm) to hold a cold core able to produce substantial basal ice formation. On the other hand, sea ice could form at the edge of the hole dug to deploy the instruments owing to horizontal heat flux, as the latter were only partially filled with ice. This possibility was tested by solving numerically the time-dependent heat equation in cylindrical coordinates. Thermal properties of sea ice were taken according to *Bitz and Lipscomb* [1999]. Boundary conditions for temperature were set to the freezing temperature of the seawater, $T_f=-1.9$ °C at the edge of the hole and at −5 °C for the far field, while the initial temperature field in the ice was assumed homogeneous and set to −5 °C. After 2 h (time elapsed between instrument deployment and the beginning of measurements), the growth of the ice at the edge of the hole is 2.5 mm, obtained by dividing the conductive heat flux at the inner boundary by the latent heat of solidification of the ice. Note that this estimate is probably an upper bound, as the initial temperature and the constant far-field temperature were both set at a

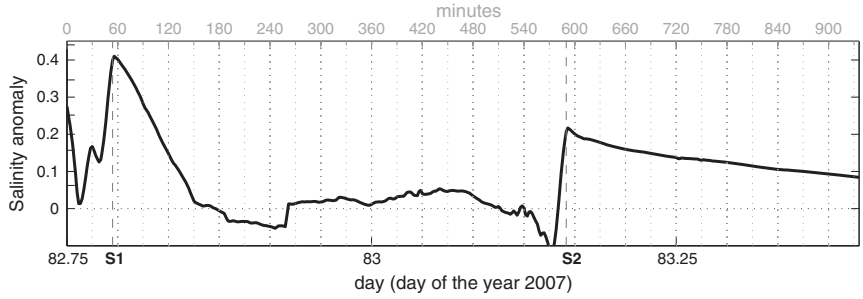

Figure 4. Salinity anomaly measured 1.4 m below the sea ice with respect to the average salinity over the first 2 days of 35.17.

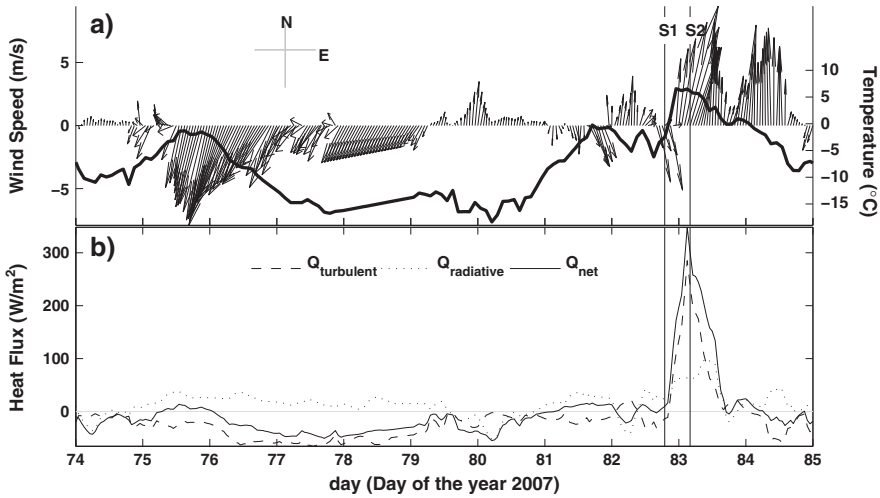

Figure 5. Time series of (a) wind (black arrows) and air temperature (solid line), (b) radiative, turbulent, and net heat flux. The vertical solid lines identify the two salinity events (*S*1 and *S*2).

conservative −5 °C for the entire thickness of the ice. In fact, the ice temperature most likely ranged between −1.9 °C at the ocean-ice interface and −5 °C or warmer at the surface, given atmospheric conditions. An ice growth of 2.5 mm around the hole implies a seawater salinity anomaly of 0.09, assuming mixing down to 1.4 m (depth where the salinity increase is observed, thus a conservative choice), so that refreezing at the edge of the hole cannot account for the observed signal. The slush used to partially fill the hole, which presents a larger surface of contact with seawater, could also contribute to the salinity anomaly through refreezing, a contribution difficult to estimate since neither the volume nor the initial temperature of this snow-ice mixture was measured. It is nevertheless possible that this contribution is substantial, but we show below that other explanations are quite likely.

[36] Alternatively, the brine release could originate from a desalination of the existing sea ice. Assuming salt conservation between sea ice of thickness h_i and a well-mixed underlying water layer of thickness h_w, the change in the bulk salinity of the sea-ice, ΔS_i (desalination), relates to the increase in salinity of the sea water, ΔS_w, according to

$$\Delta S_i = \frac{\rho_w \Delta S_w h_w}{\rho_i h_i}, \tag{4}$$

where ρ_w=1028 kg m^{-3} is the sea water density and ρ_i is the ice density taken as the fresh-water ice value (917 kg m^{-3}) in the absence of measurements (an error of ~5%). If we assume mixing of the brine down to the first salinity sensor, that is h_w=1.4 m, our observed salinity increase, ΔS_w=0.41, corresponds to a desalination of 1.5 of the sea ice. If we assume instead that mixing takes place further down, almost at the next sensor at 10 m (where the salinity increase is barely observed), that is, h_w=9.6 m, the corresponding sea-ice desalination would be as large as 11. The question is whether first-year sea ice is initially salty enough to lose salt in such proportions. According to the literature, the bulk salinity of first-year sea ice ranges from ≈5 to 12 [e.g., *Cox and Weeks*, 1974; *Kovacs*, 1996; *Notz and Worster*, 2008] and can even reach salinities as large as 25 [*Malmgren*, 1927]. Unfortunately, sea-ice bulk salinity was not measured during the deployment. At the same time of the year, in April 2001, *Skogseth et al.* [2004] report a mean salinity of 8.5 from ice cores during field work in Storfjorden. This simple calculation therefore suggests that the observed anomaly in salinity is compatible with desalination of first-year sea ice.

[37] We first investigate whether these anomalies are associated with flushing. Late on day 82, the atmosphere starts heating the snow, reaching a maximum rate of 300 W m^{-2} on day 83 (Figures 5a and 5b). Integrating this heat flux (assuming an initial snow temperature of 0 °C) yields a maximum melt rate of 0.001 kg m^{-2} s^{-1} about 1.5 h before *S*2 (red line in Figure 6). According to Darcy's law [*Eicken et al.*, 2002], the e-folding draining time would be 2 h for a permeability of 10^{-11} m^2 (e≈8%), a value consistent with spring conditions. Thermistors near the snow-ice interface (t5 and t6 in Figures 3 and 6) show a sudden warming consistent with the presence of fresher water (with a warmer freezing point). Flushing is therefore likely the cause of *S*2 but cannot explain *S*1, as snow had not yet started to melt.

[38] The only other desalination process that could explain *S*1 is gravity drainage. This process requires cold temperatures on top to destabilize the brine, conditions that were not observed during deployment, but which occurred a few days before *S*1. Whether *S*1 is compatible with gravity drainage is investigated hereafter using the 1-D halo-thermodynamic sea-ice model introduced in section 3.

4.2. Model Simulations

[39] The model parameters, especially regarding the halodynamic module, are identical to those used for the idealized simulations presented in section 3. In order to minimize the impact of errors on the initial conditions for sea ice, which are not well constrained, we started simulations 10 days before the first observation was made, using forcings described in section 4.1.1. This is sufficient given the characteristic time scale of heat diffusion within sea ice and snow (~1–2 days).

[40] The initial conditions for ice thickness and snow depth, 10 days before deployment, are not known. These were adjusted to 33 cm and 6.5 cm, respectively, so as to match observed values on day 82.75, after 10 days of simulation (40 cm thick ice, 20 cm of snow, positive freeboard). Initial S_i

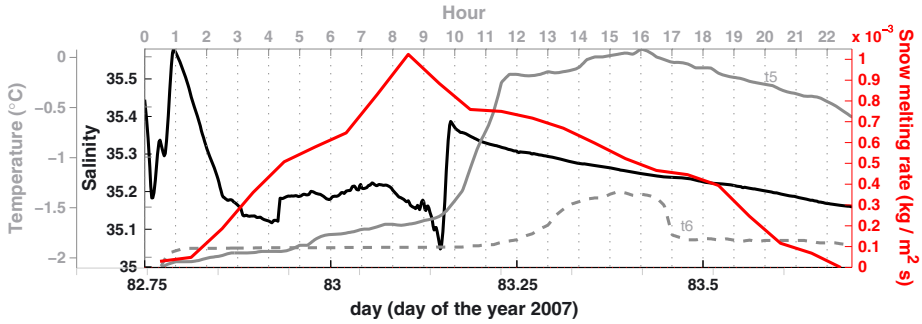

Figure 6. Evolution of salinity at 1.4 m below the ice (black line), temperature (gray lines) from the thermistors 5 cm above and 7 cm below the ice surface (t5 and t6, see Figure 3) and the snow melting rate (red line).

was arbitrarily set to 10 (a realistic value for experimental conditions), and we discuss additional simulations with different values for initial salinity.

[41] The simulated ice temperature (Figure 7b) is consistent with the evolution of the atmospheric forcing. The air temperature starts to decrease on day 76, inducing a cooling of the ice from the top, progressing downward by conduction (Figure 7a). The surface ice temperature decreases from about −2.5 °C down to ∼−5 °C. Likewise, the atmospheric warming starting on day 80.5 is accompanied by a warming

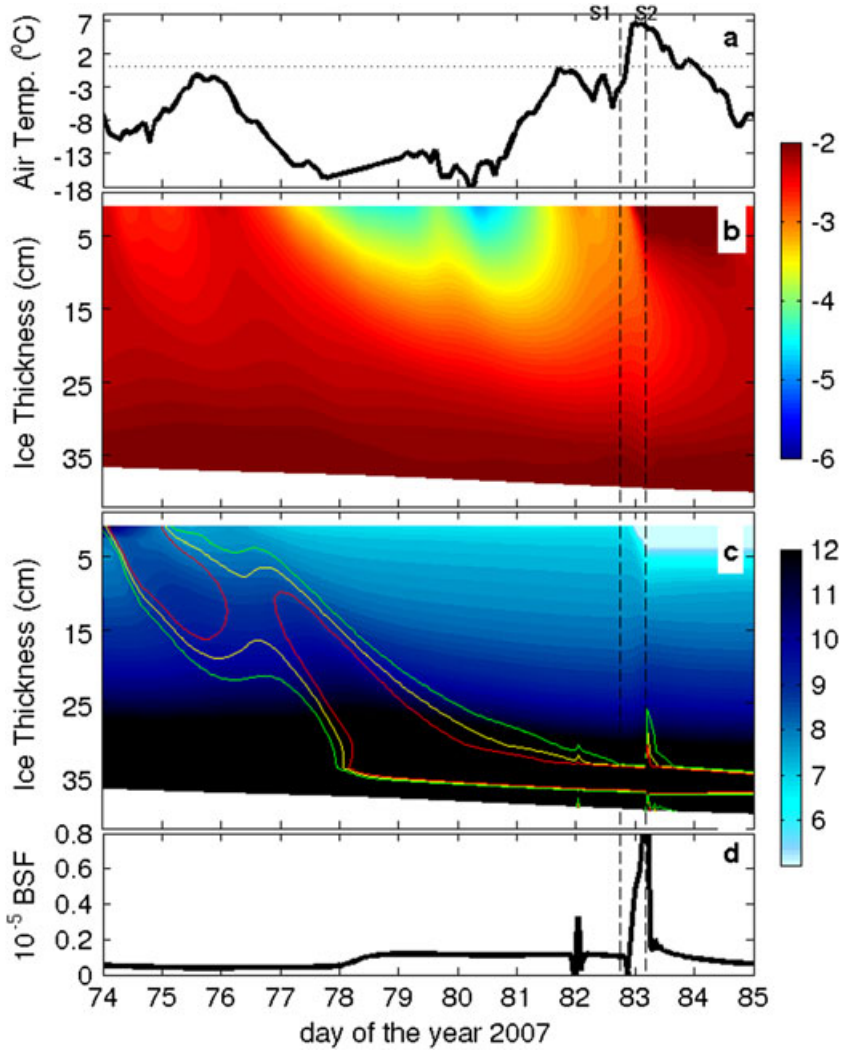

Figure 7. Temporal evolution of (a) in situ air temperature (°C), (b) simulated sea-ice temperature (°C), (c) simulated bulk ice salinity with superimposed contours of Rayleigh number equal to 10 (red line), 9.5 (yellow line) and 9 (green line), and (d) simulated basal salt flux (BSF; kg $m^{-2}s^{-1}$]). The vertical dashed lines denote the two salinity events (*S*1 and *S*2).

of the ice, which reaches a near surface maximum of ~−1.9° C during *S*2. The temperature of the ice is unfortunately not available at the time of this simulation to assess the accuracy of the model, as it took several days after deployment for the hole to refreeze (thermistors located below t5 and t6 shown in Figure 6 all measure seawater temperature). Nevertheless, the model has already been compared against in situ thermal measurements in previous work [*Vancoppenolle et al*., 2007].

[42] The simulated S_i and basal salt flux are shown in Figures 7c and 7d, respectively, starting on day 74. The peak in the salt flux on day 83 (Figure 7c), synchronous with *S*2, which we previously attributed to flushing, is striking. The model supports that flushing happens, as confirmed by the amount of snow melted in the model (not shown), and the maximal near-surface desalination (Figure 7c). Interestingly, immediately after episode *S*2, the uppermost ice layer becomes impermeable on day 83.17 owing to the input of freshwater, while until then the brine volume fraction output by the model shows that the permeability condition ($e>5\%$) was satisfied throughout the full depth of the ice (not shown). This closure of the brine network at the surface explains why flushing stops rapidly, both in the model and in observations.

[43] In addition to this signal, and quite remarkably, Figure 7c shows a desalination starting on day 77 and progressing downward from the top of the ice, similar to that discussed in the idealized simulations of section 3. It occurs in the wake of the $Ra=Ra_c$ contour, hence triggered by gravity drainage. The Ra_c contour reaches close to the ice bottom as of day 78, the time at which the basal brine release gradually increases (Figure 7d). In contrast to the observations, there is therefore no sporadic increase in the ice-ocean salt flux, which instead gradually increases, except for a small burst on day 82 associated with a convective event confined within a few centimeters above the ice bottom associated with the isoline $Ra=9$. For such values, the model indeed starts mimicking brine convection since, as explained in section 3, the transition of $D_\sigma(Ra)$ around $Ra=10$ is continuous (hyperbolic tangent) and the vertical salt diffusivity is therefore already much larger than the molecular value. In the model, the overall gradual release of salt in the model may be an artifact of the diffusive formulation of convection (3), where Ra and thus $D_\sigma(Ra)$ are computed locally at each time step. Thus, near the ice base, a supercritical Ra is hardly reached despite the inflow of salty brine from above, because the elevation tends to zero. Contrary to the flushing episode *S*2, the simulation fails to reproduce exactly the *S*1 peak apparent in Figure 4, but quite importantly shows that salt has accumulated near the ice base (gradually rejected by diffusion) owing to gravity drainage during the few days preceding this event, making gravity drainage the likely explanation. In this respect, the decrease in salinity that preceded *S*1 (Figure 4) could be interpreted as the trailing edge of a preceding sporadic salt rejection.

[44] Quantitatively, an integration of the basal salt flux from day 78 to day 83 (occurrence of *S*1) yields a mass of $0.7\,\mathrm{kg\,m^{-2}}$ of salt rejected (not shown), which translates to a seawater salinity anomaly of $0.7/h_{\mathrm{mix}}$, where h_{mix} is the depth in meters of the water layer over which the salt is being mixed. For $h_{\mathrm{mix}}=2\,\mathrm{m}$, we get an anomaly of 0.35 in good agreement with the magnitude of *S*1. Likewise, integrating the basal salt flux associated with the flushing episode (from day 83 to day 84) leads to a mass of salt of $0.3\,\mathrm{kg\,m^{-2}}$, giving a seawater anomaly of 0.15, comparable with the magnitude of *S*2.

[45] Finally, in order to test the impact of initial conditions, additional simulations with initial salinities $S_i(t_0)$ equal to 6, 7, 8, and 9 were performed. Brine convection over the entire 40 cm ice column occurs for an initial S_i of at least 8 (not shown), as predicted by the theoretical analysis (Figure 1b). As in our reference run with $S_i(t_0)=10$, these are characterized by a supercritical Ra region that reaches the ice bottom. The minimal salinity of 8 required for convection is consistent with the value of 8.5 measured by *Skogseth et al*. [2004].

5. Summary and Concluding Remarks

[46] In this contribution, based on theory, simulations and observations, we have argued that first-year sea ice can undergo substantial desalination when it is warm enough, and well before summer melt, through gravity drainage progressing throughout the full thickness of the ice. This cascade of brine is triggered when ice temperature exceeds a threshold depending on thickness and bulk salinity. This condition stems from a theoretical analysis (section 2) based on the porous-medium Rayleigh number, Ra. The latter describes the propensity of brine convection, which occurs when Ra reaches a critical value of $Ra_c\approx10$. Ra is proportional to the potential energy and to the cube of porosity. Both terms respond to temperature changes but in an opposite way. Cold temperatures enhance potential energy of brine while reducing porosity. From these competing effects, it appears that convection can develop over the entire ice only within a specific temperature range. Indeed, expressing Ra as a function of T_i, the bundle of $Ra(T_i)$ curves (for different S_i and h_i) all show the same variation, increasing with T_i until reaching a maximum before decreasing abruptly. Therefore, by imposing a threshold $Ra=Ra_c$, we define a temperature range $[T_0,T_1]$ outside of which convection is impossible.

[47] Convection will therefore be possible over the entire ice thickness once its surface temperature exceeds the threshold $T_0(S_i,h_i)$. There is thus some similarity in this mechanism with the critical thickness required for the onset of convection in growing ice, as evidenced in laboratory experiments [*Wettlaufer et al*., 1997a]. In the latter case, however, it is the increase in the brine's potential energy that triggers convection; while in the former, it is the decrease in dissipated energy as the temperature increases which is at play. The value of the temperature threshold T_0 is conveniently reported in Figure 1b for different bulk salinities and ice thicknesses. Additionally, this figure shows that this convection threshold is well above the temperature warranting sea-ice permeability (corresponding to $e>5\%$).

[48] The theoretical argument is supported by idealized simulation from a 1-D sea-ice model with advanced salt dynamics [*Vancoppenolle et al*., 2010], where the air temperature used in the forcing is adjusted to control the ice temperature. Remarkably, simulations show a rapidly developing cascade of brine through the entire ice layer, yielding a peak in the ice-ocean salt flux. Sea ice desalinates in this way by ~3.5. This cascade occurs only when surface ice temperature is warm enough, as posited by theory. The simulation

further reveals that this brine cascade is associated with a supercritical Rayleigh number, an unambiguous signature of gravity drainage.

[49] Gravity drainage has often been discussed as a wintertime desalination mechanism, as opposed to flushing by meltwater in summertime. However, in winter, cold temperatures enhance potential energy, while convection is efficiently opposed by the reduced porosity, so that gravity drainage is restricted to the bottom layers of the ice as seen in the observations of *Trodahl et al*. [2000] or *Pringle et al*. [2007].

[50] There are only a few observations of desalination in warming ice, however, which pertain to the existence of the full-depth convection mechanism discussed here. *Pringle et al*. [2007] discussed one convective episode developing over 0.8 m in 1.30 m thick warmer ice, but it was apparently confined to the ice interior and did not lead to significant brine release [*Backstrom and Eicken*, 2006]. The downward displacement of entrapped brine through the ice in warm conditions had also been reported earlier by *Kovacs* [1996]. He presented these observations in terms of a salinity migration wave, the amplitude of which diminishes with depth. This may well be a mechanism similar to the process presented in this paper; however, no evidence of substantial brine rejection out of the ice was reported. Also, from *Doronin and Kheisin* [1975] field work, such a migration wave was reported to migrate downward at about 0.8 cm/day, allowing the relative salinity maximum in the 1.20 m thick ice to drop by 17 cm in 23 days. This number is, however, much slower than the mechanism discussed here.

[51] In Storfjorden (Svalbard) in March 2007, we fortuitously recorded two intriguing salinity bursts 1.4 m below the 40 cm thick ice, during a warm storm. The first and most intense seawater salinity anomaly reached 0.41, while the second peaked at 0.21, 10 h later. A bundle of evidence, based on data analysis and simulations with the 1-D halothermodynamic sea-ice model forced with observed atmospheric conditions, suggests that the brine release signals are consistent with gravity drainage for the first salinity outburst and caused by the flushing of brine by meltwater for the second (section 4). Regarding the flushing episode, the timing of the brine rejection in the model and observations remarkably matches. The model also does simulate a cascade of salt within the ice caused by gravity drainage (Figure 7c), starting several days earlier, but reaching the base of the ice approximately when the first salinity anomaly is recorded. This episode of gravity drainage occurs throughout the entire ice, reducing the bulk salinity by 3 (observations suggest a loss ranging between 1.5 and 11.2 assuming different mixing depths). However, the simulation yields a smooth increase in the basal salt flux over several days, while the observed brine release is sporadic. Among possible reasons for this discrepancy is the model formulation of salt dynamics, in particular the representation of convection as a diffusive process, although the full-depth convective episode of the idealized simulation leads to a relatively sharp pulse in the basal flux. Additionally, uncertainties in forcings probably contribute to timing differences.

[52] Finally, the limits of a 1-D model should also be underlined, since once the ice has reached a critical thickness, the drainage process is dominated by brine channels. Recent theoretical works by *Wells et al*. [2011] find that convection controlled by brine channels yields a flux that increases approximately linearly with *Ra*, for supercritical *Ra* up to 60.

[53] While they motivated the present analysis, these serendipitous observations are not complete enough to provide an indisputable proof of desalination caused by full-depth convection, as other possible explanations cannot be totally ruled out in the absence of direct measurements within the ice. These observations can therefore only be viewed as a possible example, prompting further analysis of existing databases or future dedicated field experiments.

[54] In this respect, the substantial brine release observed in warming ice by *Widell et al*. [2006] is noteworthy. It, however, appeared to be correlated with the ocean-ice heat flux, and these authors argued that warm water could prevent refreezing of brine channels, maintaining convection. This mechanism does not seem at play in our observations, in which no heat is available from the ocean. Likewise the ocean-ice heat flux plays no role in the mechanism reported here.

[55] Ice rejects most of its salt during growth. Our analyses suggest that it loses a substantial fraction of the remnant salt immediately after the winter growth season, once the ice becomes warm enough to exceed the temperature threshold needed to trigger convection through the entire ice column. As this sequence of atmospheric conditions is fairly general, this rapid desalination process is likely to hold for large spatial scales in the Arctic.

[56] Such full-depth convective events could be important in regard to the material and gas exchanges at the ocean-ice-atmosphere interface. First, in spring, nutrients are easily exhausted by growing ice algae. In this case, any full-depth convection event would replenish nutrients by mixing nutrient-rich seawater with nutrient-depleted brine within the ice. In turn, this would promote further algal growth [see *Vancoppenolle et al*., 2010 for a discussion]. This is consistent with observations of the colonization of inner ice by algae in late spring (Zhou et al., Brine dynamics across seasons traced by sea-ice biogeochemistry, manuscript in preparation, 2013). In addition, full-depth convection would enhance gas exchange throughout the sea ice, which has been observed in spring for CO_2 [e.g., *Geilfus et al*., 2012]. However, because of the sporadic nature of the simulated convective events, we argue that those would be hard to detect in nature using ice core-based salinity and temperature measurements. Sea-ice cores give only a snapshot of variables that are highly time dependent.

[57] Finally, the frequency of full-depth convective events is likely to increase in the future Arctic Ocean. In the 20th century, the Arctic was dominated by old, relatively fresh, multi-year ice. Recent observations and climate projections indicate that a transition toward a more saline first-year ice pack is occurring [*Holland et al*., 2006; *Maslanik et al*., 2007; *Vancoppenolle et al*., 2009]. Recent observations by *Maslanik et al*. [2011] indicate that first-year ice already accounts for 55% of the total sea-ice extent in spring. Only salty first-year ice should be prone to full-depth convective events. Therefore, more first-year ice means more episodes of intense and sporadic ice-ocean salt rejection. Those episodes would increasingly affect the upper Arctic Ocean, especially in spring, when the seasonal warming of sea ice occurs. Those episodes could even perturb the vertical stability of the upper ocean, deepen and thus warm the mixed layer just before melt onset, intensify the ocean-to-ice heat flux, as well

as basal melt, and thus add to the ice-albedo feedback—to what extent remains to be determined. In current large-scale sea ice-ocean models, the effect of full depth brine convection events in sea ice is not represented. Those models typically represent the salt flux from growing sea ice as proportional to the ice growth rate [*Tartinville et al.*, 2001]. Hence, in spring, at a time when the ice is slowly growing, the models simulate an ice-ocean salt flux that by no means could present the sporadic and intense peaks suggested by the present analysis.

[58] **Acknowledgments.** Data were collected as part of the Ice-Dyn campaign funded by IPEV (prog 1058) and analyses were carried out as part of the OPTIMISM project (ANR-09-BLAN-0227-01; IPEV 1015). We warmly thank the crew of the polar yacht Vagabond, supported by the DAMOCLES programme, for their help during field work, as well as Soula Stefanopoulos for proofreading the manuscript. FJ is supported by the EU AlBan programme, scholarship E07D403997AR, with additional support from CNES. We thank Associate Editor J. Stroeve and anonymous reviewers for their valuable comments.

References

Assur, A. (1958), Composition of sea ice and its tensile strength, in Arctic Sea Ice, vol. *598*, edited by N. A. of Sciences, pp. 106–138, Maryland.

Backstrom, G. E., and H. Eicken (2006), Capacitance probe measurements of brine volume and bulk salinity in first-year sea ice, *Cold Reg. Sci. Technol.*, *46*, 167–180.

Berliand, M. E., and T. G. Berliand (1952), Determining the net long-wave radiation of the Earth with consideration of the effect of cloudiness (in Russian), *Izv. Akad. Nauk, Ser. Fiz.*, *1*, 64–78.

Bitz, C., and W. H. Lipscomb (1999), An energy-conserving thermodynamic model of sea ice, *J. Geophys. Res.*, *104*(C7), 15,669–15,677.

Carman, P. C. (1937), Fluid flow through granular beds, *Trans. Inst. Chem. Eng., London*, *15*, 150–166.

Comiso, J. C. (2002), A rapidly declining perennial sea ice cover in the Arctic, *Geophys. Res. Lett.*, *29*(20), doi:10.1029/2002GL015650.

Comiso, J. C., C. L. Parkinson, R. Gersten, and L. Stock (2008), Accelerated decline in the Arctic sea ice cover, *Geophys. Res. Lett.*, *35*(1), doi:10.1029/2007GL031972.

Cox, G. F., and W. F. Weeks (1974), Salinity variations in sea ice, *J. Glaciol.*, *13*, 109–120.

Cox, G. F., and W. F. Weeks (1988), Numerical simulations of the profile properties of undeformed first-year sea ice during the growth season, *J. Geophys. Res.*, *93*(C10), 12,499–12,460, doi:10.1029/JC093iC10p12449.

Doronin, Y. P., and D. E. Kheisin (1975), *Sea Ice*, Gidrometeoizdat Publishers, Leningrad.

Eicken, H., H. R. Krouse, D. Kadko, and D. K. Perovich (2002), Tracer studies of pathways and rates of meltwater transport through Arctic summer sea ice, *J. Geophys. Res.*, *107*(C10,8046), doi:10.1029/2000JC000583.

Eide, L., and S. Martin (1975), The formation of brine drainage features in young sea ice, *J. Glacio.*, *14*(70), 137–154.

Feltham, D. L., N. Untersteiner, J. S. Wettlaufer, and M. G. Worster (2006), Sea ice is a mushy layer, *Geophys. Res. Lett.*, *33*(L14501), doi:10.1029/2006GL026290.

Freitag, J. (1999), Untersuchungen zur Hydrologie des arktischen Meereises-Konseauenzen für den kleinskaligen Stofftransport (in German), *Ber. Polarforsch.*, *325*, 150.

Freitag, J., and H. Eicken (2003), Meltwater circulation and permeability of Arctic summer sea ice derived from hydrological field experiments, *J. Glaciol.*, *49*(166), 349–358.

Geilfus, N.-X., G. Carnat, T. Papakyriakou, J.-L. Tison, B. Else, H. Thomas, E. H. Shadwick, and B. Delille (2012), PCO2 dynamics and related air-ice CO2 fluxes in the Arctic coastal zone (Amundsen Gulf, Beaufort Sea), *J. Geophys. Res.*, doi:10.1016/2011JC007118.

Golden, K. M., S. F. Ackley, and V. I. Lytle (1998), The percolation phase transition in sea ice, *Science*, *282*, 2238–2241.

Golden, K. M., H. Eicken, A. L. Heaton, J. Miner, D. J. Pringles, and J. Zhu (2007), Thermal evolution of permeability and microstructure in sea ice, *Geophys. Res. Lett.*, *34*(L16501), doi:10.1029/2007GL030447.

Goosse, H. (1997), Modeling the large-scale behavior of the coupled ocean-sea ice system, Ph.D. thesis, Université Catholique de Louvain.

Haarpaintner, J., J. Gascard, and P. Haugan (2001), Ice production and brine formation in Storfjorden, Svalbard, *J. Geophys. Res.*, *106*, 1–13.

Haas, C., S. Hendricks, H. Eicken, and A. Herber (2010), Synoptic airborne thickness surveys reveal state of Arctic sea ice cover, *Geophys. Res. Lett.*, *37*, L09,501, doi:10.1029/2010GL042652.

Holland, M. M., C. M. Bitz, E. C. Hunke, W. H. Lipscomb, and J. Schramm (2006), Influence of the sea ice thickness distribution on polar climate in CCSM3, *J. Clim.*, *19*, 2398–2414.

Hudier, E. J.-J., R. G. Ingram, and K. Shirasawa (1995), Upward flushing of sea water through first year ice, *Atmos. Ocean*, *33*(3), 569–580.

Hunke, E. C., D. Notz, A. K. Turner, and M. Vancoppenolle (2001), The multiphase physics of sea ice: A review for model developers, *The Cryosphere*, *5*, 989–1009, doi:10.5194/tc-5-989-2011.

Jardon, F. P., P. Bouruet-Aubertot, Y. Cuypers, F. Vivier, and A. Lourenço (2011), Internal waves and vertical mixing in the Storfjorden Polynya, Svalbard, *J. Geophys. Res.*, *116*(C12040), doi:10.1029/2010JC006918.

Jardon, F. P., F. Vivier, P. Bouruet-Aubertot, A. Lourenço, and Y. Cuypers (2012), Ice production in Storfjorden, Svalbard, from a model based AMSR-E observations, *J. Geophys. Res.*, in revision.

Kovacs, A. (1996), Sea ice, part i, bulk salinity versus ice floe thickness, *CRREL Report*, *96*(7), 16.

Kozeny, J. (1927), Ueber kapillare leintung des wassers im boden, *Sitzungsber Akad. Wiss.*, *136*(2a), 271–306.

Kwok, R., and D. A. Rothrock (2009), Decline in Arctic sea ice thickness from submarine and ICESat records: 1958–2008, *Geophys. Res. Lett.*, *36*, doi:10.1029/2009GL039035.

Lake, R., and E. L. Lewis (1970), Salt rejection by sea ice during growth, *J. Geophys. Res.*, *75*(3), 583–597.

Lytle, V. I., and S. F. Ackley (1996), Heat flux through sea ice in the western Weddell Sea: Convective and conductive transfer processes, *J. Phys. Oceanogr.*, *101*(C4), 8853–8868.

Malmgren, F. (1927), On the properties of sea ice in The Norwegian Polar Expedition "Maud", *Sci. Results*, *1*, 1–67.

Maslanik, J., J. Stroeve, C. Fowler, and W. Emery (2011), Distribution and trends in Arctic sea ice age through spring 2011, *Geophys. Res. Lett.*, *38*, doi:10.1029/2011GL047735.

Maslanik, J. A., C. Fowler, J. Stroeve, S. Drobot, J. Zwally, D. Yi, and W. Emery (2007), A younger, thinner Arctic ice cover: Increased potential for rapid, extensive sea ice loss, *Geophys. Res. Lett.*, *34*, L24,501, doi:10.1029/2010GL032043.

Maykut, G. A. (1982), Large-scale heat exchange and ice production in the central Arctic, *J. Geophys. Res.*, *87*(C10), 7971–7984.

Nghiem, S. V., I. G. Rigor, D. K. Perovich, P. Clemente-Colón, J. W. Weatherly, and G. Neumann (2007), Rapid reduction of Arctic perennial sea ice, *Geophys. Res. Lett.*, *34*(L19504), doi:10.1029/2007GL031138.

Notz, D., and G. Worster (2008), In situ measurements of the evolution of young sea ice, *J. Geophys. Res.*, *113*(C03001), doi:10.1029/2007JC004333.

Notz, D., and G. Worster (2009), Desalination processes of sea ice revisited, *J. Geophys. Res.*, *114*(C05006), doi:10.1029/2008JC004885.

Parkinson, C. L., and W. M. Washington (1979), A large-scale numerical model of sea ice, *J. Geophys. Res.*, *84*(C1), 311–336.

Perovich, D. K., T. C. Grenfell, B. Light, and P. V. Hobbs (2002), Seasonal evolution of the albedo of multiyear Arctic sea ice, *J. Geophys. Res.*, *107*(C10), 8044, doi:10.1029/2000JC000438.

Perovich, D. K., S. V. Nghiem, T. Markus, and A. Schweiger (2007), Seasonal evolution and interannual variability of the local solar energy absorbed by the Arctic sea ice-ocean system, *J. Geophys. Res.*, *112*(C03005), doi:10.1029/2006JC003558.

Polashenski, D. C., and D. Perovich, J. Richter-Menge, and B. Elder (2011), Seasonal ice mass-balance buoys: Adapting tools to the changing Arctic, *Ann. Glaciol.*, *52*(57), 989–1009.

Pringle, D. J., H. Eicken, H. J. Trodahl, and L. G. E. Backstrom (2007), Thermal conductivity of landfast Antarctic and Arctic sea ice, *J. Geophys. Res.*, *112*, doi:10.1029/2006JC003641.

Rigor, I. G., and J. M. Wallace (2004), Variations in the age of Arctic sea-ice and summer sea-ice extent, *Geophys. Res. Lett.*, *31*(L09401), doi:10.1029/2004GL019492.

Shine, K. (1984), Parameterization of the short wave flux over high albedo surfaces as a function of cloud thickness and surface albedo, *Q. J. R. Meteorol. Soc.*, *110*, 747–764.

Simmons, A., S. Uppala, D. Dee, and S. Kobayashi (2006), ERA-Interim: New ECMWF reanalysis products from 1989 onwards, *ECMWF Newsletter*, *110*, 25–35.

Skogseth, R., P. Haugan, and J. Haarpainter (2004), Ice and brine production in Storfjorden from four winters of satellite and in situ observations and modeling, *J. Geophys. Research*, *109*(C10008), doi:10.1029/2004JC002384.

Skogseth, R., F. Nilsen, and L. H. Smedsrud (2009), Supercooled water in an Arctic polynya: Observations and modeling, *J. Glaciol.*, *55*(189), 43–52.

Stroeve, J. L., M. Holland, W. Meier, T. Scambos, and M. Serreze (2007), Arctic sea ice decline: Faster than forecast, *Geophys. Res. Lett.*, *34*(L09501), doi:10.1029/2007GL029703.

Tartinville, B., J. M. Campin, T. Fichefet, and H. Goosse (2001), Realistic representation of the surface freshwater flux in an ice-ocean general circulation model, *Ocean Model*, *3*(1-2), 95–108.

Trodahl, H. J., M. J. McGuinnes, P. J. Langhorne, K. Collins, A. E. Pantoja, I. J. Smith, and T. G. Haskell (2000), Heat transport in McMurdo Sound first-year fast ice, *J. Geophys. Res.*, *105*(C5), 11,347–11,358, doi:10.1029/1999JC000003.

Untersteiner, N. (1968), Natural desalination and equilibrium salinity profile of perennial sea ice, *J. Geophys. Res.*, *73*(4), 1251–1257.

Vancoppenolle, M., C. M. Bitz, and T. Fichefet (2007), Summer landfast sea ice desalination at Point Barrow, Alaska: Modeling and observations, *J. Geophys. Res.*, *112*(C04022), doi:10.1029/2006JC0034.

Vancoppenolle, M., T. Fichefet, H. Goosse, S. Bouillon, G. Madec, and M. Morales Maqueda (2009), Simulating the mass balance and salinity of Arctic and Antarctic sea ice. 1. Model description and validation, *Ocean Modell.*, *27*, 33–53, doi:10.1016/j.ocemod.2008.10.005.

Vancoppenolle, M., H. Goosse, A. de Montely, T. Fichefet, B. Tremblay, and J. L. Tison (2010), Modelling brine and nutrient dynamics in Antarctica sea ice: The case of dissolved silica, *J. Geophys. Res.*, *115*(C02005), doi:10.1029/2009JC005369.

Vancoppenolle, M., et al. (2011), Assessment of radiation forcing data sets for large-scale sea ice models in the southern ocean, *Deep Sea Res. II*, *58*, 1237–1249, doi:10.1016/j.dsr2.2010.10.039.

Vivier, F., A. Lourenço, et al. (2013), "Ice-T": An autonomous buoy to measure ice thickness and thermal fluxes in sea ice, *J. Atmos. Ocean. Tech.*, in prep.

Weeks, W. F. (2010), On Sea Ice, Univ. of Alaska Press, Fairbanks, Alaska.

Weeks, W. F., and S. F. Ackley (1986), The growth, structure and properties of sea ice. In: The Geophysics of Sea Ice, Edited by N Untersteiner, Plenum Press, New York.

Wells, A. J., J. S. Wettlaufer, and S. A. Orszag (2011), Brine fluxes from growing sea ice, *Geophys. Res. Lett.*, *38*(L04501), doi:10.1029/2010GL046288.

Wettlaufer, J. S., M. G. Worster, and H. E. Huppert (1997a), The phase evolution of young sea ice, *Geophys. Res. Lett.*, *24*(10), 1251–1254.

Wettlaufer, J. S., M. G. Worster, and H. E. Huppert (1997b), Natural convection during solidification of an alloy from above with application to the evolution of sea ice, *J. Fluid Mech.*, *344*, 291–316.

Widell, K., I. Fer, and P. M. Haugan (2006), Salt release from warming sea ice, *Geophys. Res. Lett.*, *33*(L12501), doi:10.1029/2006GL026262.

Worster, M. G. (1992), Interactive Dynamics of Convection and Solidification, chap. The dynamics of mushy layers, pp. 113–138, Springer, New York, Kluwer Acad., Norwell, Mass.

Worster, M. G. (1997), Convection in a Mushy Layer, *J. Fluid Mech.*, *29*, 91–122.